Chapter 3

Analytical Correction of Rotational Motion Artifacts

3.1 Introduction

In this chapter, the effect of rotational motion on k-space MR data is analyzed, and a general rotational motion model for in-plane rigid rotations is developed. It is shown that in-plane rigid rotations around arbitrary points in the field of view (FOV) can be modelled by separate 2D translations and rotations around the origin [78]. Since the correction techniques for translational motion artifacts are well established as shown by scores of publications [51]-[77], this chapter will only deal with artifacts caused by the rotational component around the slice selection axis.

The term analytical correction algorithm is used to describe algorithms where a closed form solution allows the direct calculation of the corrected data. This is in contrast to iterative correction algorithms that iteratively improve an estimate

of the corrected data. Due to the scale of the problem, analytical algorithms can only be used when the problem is reduced to a set of linear equations.

Initially, single step in-plane rotations are considered as the simplest type of rotation. The assumptions and limitations of the motion model and data correction method are discussed. As a comparatively more useful model, in-plane rotation at constant angular velocity is analyzed, and an analytical data correction technique is described. The theoretical and practical limitations of this correction algorithm is discussed in detail.

3.2 Rotational Motion Model

For planar, inter-view effect, rigid rotational motion, the relation between the points of a rotated image $m(\hat{x}, \hat{y})$ and its unrotated counterpart $m(x, y)$ can be expressed by [78]

$$\begin{pmatrix} \hat{x} - x_c \\ \hat{y} - y_c \end{pmatrix} = \begin{pmatrix} \cos\theta_r & -\sin\theta_r \\ \sin\theta_r & \cos\theta_r \end{pmatrix} \begin{pmatrix} x - x_c \\ y - y_c \end{pmatrix} \tag{3.1}$$

where $\theta_r = \theta_r(k_y)$ is the counter-clockwise angle of rotation about the slice selection direction, and $[x_c = x_c(k_y), y_c = y_c(k_y)]$ is the centre of rotation within the FOV. Under the assumption of inter-view motion, θ_r, x_c and y_c become variables of phase encode k_y only. In order to identify the rotational and translational components of the related motion, Equation 3.1 can be re-arranged as shown below:

$$\begin{pmatrix} \hat{x} \\ \hat{y} \end{pmatrix} = \begin{pmatrix} \cos\theta_r & -\sin\theta_r \\ \sin\theta_r & \cos\theta_r \end{pmatrix} \begin{pmatrix} x \\ y \end{pmatrix} + \begin{pmatrix} 1 - \cos\theta_r & \sin\theta_r \\ -\sin\theta_r & 1 - \cos\theta_r \end{pmatrix} \begin{pmatrix} x_c \\ y_c \end{pmatrix} \tag{3.2}$$

By defining the translational components $p(k_y)$ and $q(k_y)$ along the frequency encoding and phase encoding axes as

$$\begin{pmatrix} p \\ q \end{pmatrix} = \begin{pmatrix} 1-\cos\theta_r & \sin\theta_r \\ -\sin\theta_r & 1-\cos\theta_r \end{pmatrix} \begin{pmatrix} x_c \\ y_c \end{pmatrix} \tag{3.3}$$

the Equation 3.2 can be formulated as shown below:

$$\begin{pmatrix} \hat{x} \\ \hat{y} \end{pmatrix} = \begin{pmatrix} \cos\theta_r & -\sin\theta_r \\ \sin\theta_r & \cos\theta_r \end{pmatrix} \begin{pmatrix} x \\ y \end{pmatrix} + \begin{pmatrix} p \\ q \end{pmatrix} \tag{3.4}$$

Therefore, a planar rigid rotation about any arbitrary axis along the slice selection direction, through the FOV can be modelled as a combination of translational and rotational components. This separable nature of the problem can be used to simplify the correction algorithm by correcting separately for translational and rotational components. It is well known from the Fourier rotation theorem that rotation of an object around the origin of the FOV by an angle θ_r, causes the image spatial frequency components to rotate by the same angle [120]. Using this property, it is possible to write the following relation between the motion affected MR signal $S'(k_x, k_y)$ and the original $S(k_x, k_y)$, only considering the rotations around the slice selection axis. Such that,

$$S'(k_x, k_y) = S\left[k_x \cos\theta_r(k_y) + k_y \sin\theta_r(k_y), -k_x \sin\theta_r(k_y) + k_y \cos\theta_r(k_y)\right] \tag{3.5}$$

According to Equation 3.5, the above effect imposes non-uniform sampling in the k-space data. In contrast, translational components only introduce a phase error [62] given by

$$\phi(k_x, k_y) = 2\pi\left[k_x p(k_y) + k_y q(k_y)\right] \tag{3.6}$$

where $\phi(k_x, k_y)$ is the phase error introduced by the shift in the centre of rotation from the slice selection axis. By combining Equations 3.5 and 3.6, a general formulation of the effect of rotational motion around an arbitrary axis, perpendicular to the transverse plane, can be derived. If the corrupted MR k-space is defined by $\hat{S}(k_x, k_y)$, then,

$$\hat{S}(k_x, k_y) = e^{-i\phi(k_x, k_y)} S'(k_x, k_y) \tag{3.7}$$

Since algorithms for the correction of phase error $\phi(k_x, k_y)$ have been extensively studied in the past, this thesis will mainly concentrate on methods of reconstructing $S(k_x, k_y)$ from $S'(k_x, k_y)$.

3.3 Single Step Rotation

Single step rotation represents the simplest type of in-plane rotational motion. This type of motion is rarely encountered in clinical settings. However, in order to describe the steps involved in correcting the motion affected data, the simplest model is initially considered.

For single step rotation, the rotation angle $\theta_r(k_y)$ at the $k_y{}^{th}$ phase encode is given by

$$\theta_r(k_y) = \begin{cases} \theta_1 & \text{for } k_y < k_{rot} \\ \theta_2 & \text{for } k_y \geq k_{rot} \end{cases} \tag{3.8}$$

where the single step rotation occurs between the views $(k_{rot} - 1)$ and k_{rot}. If the orientation of the imaged object at the view $k_y = \left(\frac{N}{2}\right)$ is considered as the reference, then $\theta_1 = 0^o$ for $k_{rot} \geq \left(\frac{N}{2}\right)$ and $\theta_2 = 0^o$ for $k_{rot} < \left(\frac{N}{2}\right)$. Therefore, an integral part of the data correction scheme is locating the view k_{rot} at which the movement of the object occurs. In this simplest case, at least $\left(\frac{N}{2}\right)$ views of data are always unaffected by motion. The worst case scenarios are when the motion occurs between the views $\left[\left(\frac{N}{2}\right) - 1\right]$ and $\left(\frac{N}{2}\right)$ $\left(\text{i.e. } k_{rot} = \left(\frac{N}{2}\right)\right)$, or between the views $\left(\frac{N}{2}\right)$ and $\left[\left(\frac{N}{2}\right) + 1\right]$ $\left(\text{i.e. } k_{rot} = \left(\frac{N}{2}\right) + 1\right)$. In these cases, a rotation angle of 0^o is allocated to exactly $\left(\frac{N}{2}\right)$ views (i.e. views are presumed to be unaffected by motion).

Since half of the k-space data are guaranteed to be motion free, the complex conjugate symmetry of the k-space can be used for data correction [80], under strict assumptions. The above method will only be effective when there is no

concurrent translational motion or phase shifts due to magnetic field inhomogeneity. The timing of the sampling of the spin echo signal is also assumed to be phase error free. These assumptions impose strict limitations on the method of conjugate symmetry, and is generally not used for data correction and MR image reconstruction. More useful and effective methods of data correction will be discussed in the remainder of this chapter and the following chapters.

3.3.1 Detection of Rotation View and Data Correction

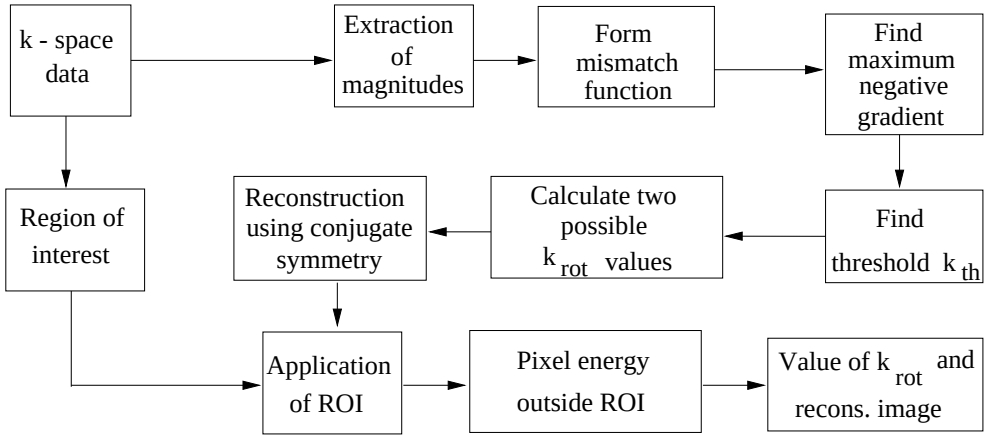

Figure 3.1: Data correction methodology for single step rotation model.

Although the conjugate symmetry of the k-space data may be violated due to phase errors, the magnitudes usually display the symmetric properties commonly found in the 2D Fourier transform. Therefore, it is observed that there is a detectable incongruity among the magnitudes of the k-space data in the vicinity of the view at which the rotation occurs. A comparison between each $k_y{}^{th}$ and $(N - k_y)^{th}$ views yield a set of *mismatch values* which can be used to identify the threshold view k_{th} where the data mismatch first occurs. This data mismatch function (DMM) is defined by

$$DMM(k_y) = \sum_{k_x=1}^{N-1} ||S'(k_x, k_y)|^2 - |S'(N - k_x, N - k_y)|^2| \qquad (3.9)$$

where $1 \leq k_y < \frac{N}{2}$.

The mismatch function (DMM) has the maximum negative gradient between the view pairs corresponding to $k_y - 1$ and k_y as given in the following equation:

$$k_{th} = \max_{k_y} [DMM(k_y - 1) - DMM(k_y)] \tag{3.10}$$

The k_{th} value indicate two possibilities for the value of k_{rot}. The relationship between k_{th} and k_{rot} is given by either $k_{rot} = k_{th}$ or $k_{rot} = N - k_{th} + 1$, depending on whether the rotation occurs before or after the view $k_y = \frac{N}{2}$ respectively. In order to resolve this ambiguity and to obtain a unique solution for k_{rot}, the energy outside the ROI of the reconstructed images is considered for both possibilities. The ROI boundary is extracted using the algorithm described in Chapter 2. The flow diagram of Figure 3.1 illustrates the steps involved in estimating the value of k_{rot} and the reconstruction of the motion corrected image, as described previously in Section 3.3.

3.4 Rotation at Constant Angular Velocity

In practice, in-plane rotations at constant angular velocity may occur due to the patients slowly rotating their head around the neck, or limb movements around the joints. However, such rotations will be accompanied by translational motion and rotations at accelerating and decelerating angular velocities. Therefore, by itself, the model introduced in this section may not be effective in correcting for all types of patient motion artifacts, which is also true for the translational model. However, by amalgamating the available models, a more useful technique for motion artifact correction can be achieved, as shown by Zoroofi et. al. [78]. Another reason for selecting this type of rotation to describe the analytical correction method is its simplicity and the ability to represent all the associated rotation angles by a single parameter.

If the object is rotating at a sufficiently slow pace, the time varying magnetization of the object can be assumed to be time invariant during the acquisition of a single view (i.e. inter-view motion). The following derivation determines the maximum constant angular velocity for no intra-view motion to occur during readout of a view:

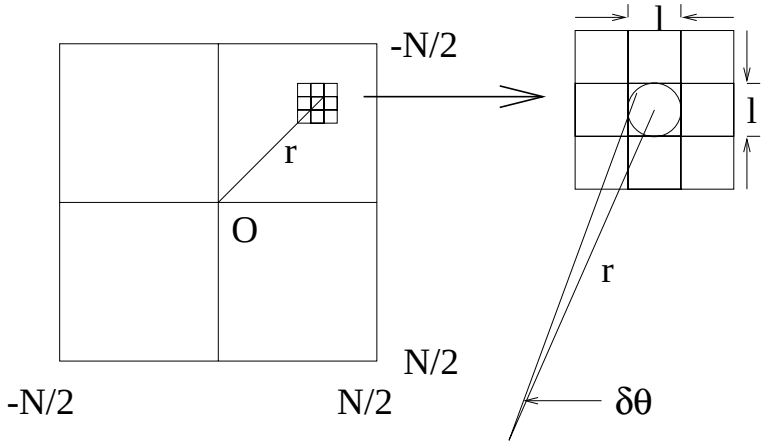

Figure 3.2: Alteration of pixel intensity due to rotation.

As shown in Figure 3.2, if the distance between the centres of two adjacent pixels is l, the pixel intensity of a given pixel, r distance away from the origin, does not change due to rotation by an angle $\delta\theta$, provided that the arc length $r\delta\theta$ is smaller than $\frac{l}{2}$. The maximum arc length occurs when

$$r = \sqrt{\left(\frac{N}{2}\right)^2 + \left(\frac{N}{2}\right)^2} = \frac{N}{\sqrt{2}} \tag{3.11}$$

Therefore, if $\frac{N}{\sqrt{2}}\delta\theta < \frac{l}{2}$, no alteration to the pixel intensity of the image would occur due to a rotation by an angle $\delta\theta$. If we take l to be equal to 1 unit, the above condition is given by

$$\delta\theta < \frac{\sqrt{2}}{2N} \tag{3.12}$$

In a typical MR scan, the repetition time (T_R) is approximately 1000ms, whereas the readout time is about 20ms. Under such conditions, the maximum angular

velocity allowable before violating the assumption of no intra-view motion is given by

$$\omega_{c\ max} = \frac{\delta\theta}{\delta t} = \frac{\sqrt{2}/(2N)}{0.02} = \frac{25\sqrt{2}}{N} \tag{3.13}$$

For $N = 256$, $\omega_{c\ max} \approx 0.13811(r/s)$. Therefore, if $\omega < 0.13811(r/s)$, the object is assumed to be moving sufficiently slowly, so that there is no detectable movement during the readout of a single view.

According to Equation 3.13, the maximum angular velocity allowable with this correction method (i.e. under the assumption of inter-view motion, 256 phase encodes and readout time of 20ms) is approximately $0.13811(r/s)$, which is equivalent to a maximum angular span of approximately $\pm 1000^o$ (i.e. $0.13811 \times \frac{180^o}{\pi} \times \pm 128$) during the entire scan. Such a speed can be useful for non-destructive testing of moving mechanical parts.

Since a human neck has a rotational freedom of less than 180 degrees, total angular span should be limited to π radians. Therefore the maximum angular velocity that can be achieved under such limitations is given by

$$\omega'_{c\ max} = \frac{\pi}{256 T_R} \approx 0.01(r/s) \tag{3.14}$$

Hence, $\omega'_{c\ max} \ll \omega_{c\ max}$ for total rotations of less than 180^o, and the condition for no intra-view motion is satisfied for all scenarios described in this section.

For rotation at constant angular velocity ω_c, the rotation angle $\theta_r(k_y)$ at the ${k_y}^{th}$ phase encode, is given by

$$\theta_r(k_y) = \omega_c k_y \tag{3.15}$$

where $k_y = -\frac{N}{2}, ..., -1, 0, 1, ..., \frac{N}{2} - 1$.

Therefore, if the new co-ordinates, due to rotational motion of the object at the ${k_y}^{th}$ phase encode are given by

$$\bar{x}(k_y) \quad = \quad x \cos\theta_r(k_y) - y \sin\theta_r(k_y) \tag{3.16}$$

$$\text{and} \qquad \bar{y}(k_y) \;=\; x\sin\theta_r(k_y) + y\cos\theta_r(k_y), \tag{3.17}$$

the corrupted MRI signal $S'(k_x, k_y)$, due to time varying magnetization can be modelled by

$$S'(k_x, k_y) = \sum_{x=-\frac{N}{2}}^{\frac{N}{2}-1} \sum_{y=-\frac{N}{2}}^{\frac{N}{2}-1} m(\bar{x}, \bar{y}) e^{-i\frac{2\pi}{N}(xk_x + yk_y)} \tag{3.18}$$

The mathematical implication of Fourier rotation theorem on Equation 3.18 is given by

$$S'(k_x, k_y) = S(\bar{k_x}, \bar{k_y}) \tag{3.19}$$

where

$$\bar{k_x} \;=\; k_x\cos\theta_r(k_y) + k_y\sin\theta_r(k_y) \tag{3.20}$$

$$\bar{k_y} \;=\; -k_x\sin\theta_r(k_y) + k_y\cos\theta_r(k_y) \tag{3.21}$$

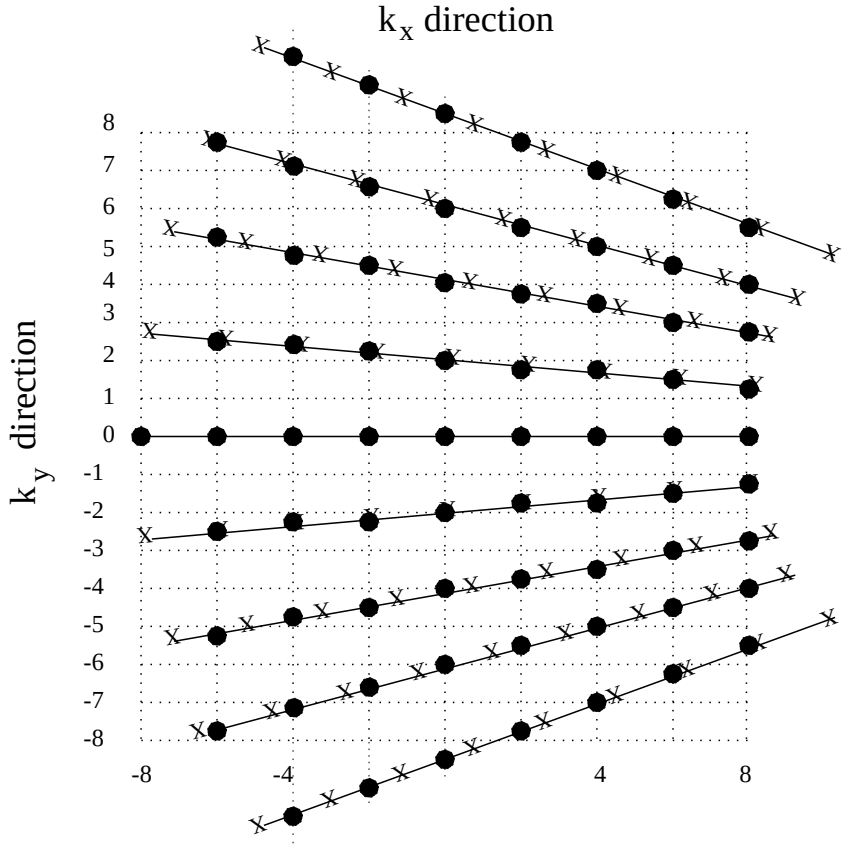

Figure 3.3: Interpolation of view data along each rotated view in the k-space.

The k-space data samples are graphically illustrated by *cross* ($\times$) marks in Figure 3.3. The skewed lines indicate the data belonging to each view, sampled from each phase encoded signal. The samples are uniformly distributed along each skewed line and the number of samples per view can be set according to the sampling speed of the system.

The k-space values at the intersections of the skewed lines with vertical grid lines in Figure 3.3 can be computed via interpolation of acquired data along each skewed line. Such interpolated values are indicated by *dot* ($\bullet$) marks in Figure 3.3. Further interpolation along vertical grid-lines leads to degradation of the final image quality, since the available values are distributed at non-uniform intervals and generated via interpolation of different view data.

The following section describes the image reconstruction algorithm, that uses the separable nature of 2D Fourier transform and the available symmetry conditions of the motion model to efficiently reconstruct the final image, preserving the image quality.

3.4.1 Image Reconstruction Algorithm

The reconstructed image is arbitrarily set to be of the magnetization of the scanned object, at its orientation during the acquisition of the $\left(\frac{N}{2}\right)^{th}$ view, which is denoted by $m(x, y)$. Therefore, the relative rotation angle associated with the ${k_y}^{th}$ view is given by $\theta_r(k_y) = \omega_c k_y$ (Equation 3.15).

Assume that each acquired view contains $N \times m$ complex data samples, where m is an appropriate integer determined according to the sampling process. The i^{th} sample of the ${k_y}^{th}$ view is represented by $D(i, k_y)$. When the view data are located on the k-space, they span on a straight line inclined at an angle $\theta_r(k_y)$ to the $k_y = 0$ line (Figure 3.3). The k-space value at the point of intersection

between the inclined line and any vertical line can be interpolated from the nearest data samples using linear interpolation, as given below:

$$D(\hat{i}, k_y) = [D(i+1, k_y) - D(i, k_y)]\,\delta + D(i, k_y) \tag{3.22}$$

where δ is given by $\delta = \hat{i} - i$, where $i < \hat{i} < (i+1)$. In order to calculate $\hat{i}$, $\bar{k}_x$ (as in Equation 3.20) is set to integer value a within the range $-\frac{N}{2}$ to $(\frac{N}{2} - 1)$ and the resulting k_x is used to evaluate $\hat{i}$ as given below:

$$\hat{i} = \frac{a - k_y \sin\theta_r(k_y)}{\cos\theta_r(k_y)} \times m \tag{3.23}$$

Each $D(\hat{i}, k_y)$ value represents a k-space value given by $S(k_x, \hat{k}_y)$ where k_x is an integer and $\hat{k}_y$ is a non-integer. The separable nature of the 2D Fourier transform enables $S(k_x, \hat{k}_y)$ to be separated as follows:

$$S(k_x, \hat{k}_y) = \sum_{y=-\frac{N}{2}}^{\frac{N}{2}-1} G(k_x, y) e^{-i\frac{2\pi}{N} y \hat{k}_y} \tag{3.24}$$

where

$$G(k_x, y) = \sum_{x=-\frac{N}{2}}^{\frac{N}{2}-1} m(x, y) e^{-i\frac{2\pi}{N} x k_x} \tag{3.25}$$

In order to evaluate $\hat{k}_y$, $\bar{k}_x$ (in Equation 3.20) is set to an integer value a within the range $-\frac{N}{2}$ to $(\frac{N}{2} - 1)$ and the Equations 3.20 and 3.21 are solved simultaneously by eliminating k_x. The resulting $\bar{k}_y$ value is taken to be $\hat{k}_y$ as given below:

$$\hat{k}_y(k_y) = \frac{k_y - a \sin\theta_r(k_y)}{\cos\theta_r(k_y)} \tag{3.26}$$

The odd symmetry of $\hat{k}_y$ about $k_y = 0$ can be utilized efficiently to compute $G(k_x, y)$.

Using the definition of 1D discrete inverse Fourier transform, Equation 3.24 can be transformed to the following result:

$$G(k_x, y) = \frac{1}{N} \sum_{k_y=-\frac{N}{2}}^{\frac{N}{2}-1} S(k_x, \hat{k}_y) e^{i\frac{2\pi}{N} y \hat{k}_y} \tag{3.27}$$

where the relationship between k_y and $\hat{k}_y$ is given in Equation 3.26. For a particular value of $\bar{k}_x = a$, Equations 3.15 and 3.26 can be combined to show that $\hat{k}_y$ posseses odd symmetry, that is

$$\hat{k}_y(-k_y) = -\hat{k}_y(k_y) \tag{3.28}$$

Therefore, using the odd symmetry of $\hat{k}_y$ given in Equation 3.28, $G(k_x, y)$ can be written as

$$G(k_x, y) = \frac{1}{N}\left[\sum_{k_y=1}^{\frac{N}{2}} S(k_x, \hat{k}_y)e^{i\frac{2\pi}{N}y\hat{k}_y} + S(k_x, -\hat{k}_y)e^{-i\frac{2\pi}{N}y\hat{k}_y}\right] + \frac{1}{N}S(k_x, 0) \tag{3.29}$$

Replacing y with $-y$ yields,

$$G(k_x, -y) = \frac{1}{N}\left[\sum_{k_y=1}^{\frac{N}{2}} S(k_x, \hat{k}_y)e^{-i\frac{2\pi}{N}y\hat{k}_y} + S(k_x, -\hat{k}_y)e^{i\frac{2\pi}{N}y\hat{k}_y}\right] + \frac{1}{N}S(k_x, 0) \tag{3.30}$$

Addition of Equations 3.29 and 3.30, and using the Eular identity gives

$$G(k_x, y) + G(k_x, -y) = \frac{2}{N}\left[\left[\sum_{k_y=1}^{\frac{N}{2}} \left[S(k_x, \hat{k}_y) + S(k_x, -\hat{k}_y)\right] \cos\left(\frac{2\pi}{N}y\hat{k}_y\right)\right] + S(k_x, 0)\right] \tag{3.31}$$

Similarly, subtraction of Equation 3.30 from 3.29, and using the Eular identity gives

$$G(k_x, y) - G(k_x, -y) = \frac{2}{N}\left[\sum_{k_y=1}^{\frac{N}{2}} i\left[S(k_x, \hat{k}_y) - S(k_x, -\hat{k}_y)\right] \sin\left(\frac{2\pi}{N}y\hat{k}_y\right)\right] \tag{3.32}$$

Let P and Q be defined as given in Equations 3.33 and 3.34 respectively:

$$P = \left[\sum_{k_y=1}^{\frac{N}{2}} \left[S(k_x, \hat{k}_y) + S(k_x, -\hat{k}_y)\right] \cos\left(\frac{2\pi}{N}y\hat{k}_y\right)\right] + S(k_x, 0) \tag{3.33}$$

$$Q = \sum_{k_y=1}^{\frac{N}{2}} i\left[S(k_x, \hat{k}_y) - S(k_x, -\hat{k}_y)\right] \sin\left(\frac{2\pi}{N}y\hat{k}_y\right) \tag{3.34}$$

Therefore, Equations 3.31 and 3.32 can be re-written as

$$G(k_x, y) + G(k_x, -y) = \frac{2P}{N} \tag{3.35}$$

$$G(k_x, y) - G(k_x, -y) = \frac{2Q}{N} \tag{3.36}$$

Addition of Equations 3.35 and 3.36 gives the result shown in Equation 3.37, whereas subtraction of Equation 3.36 from 3.35 gives the result shown in Equation 3.38. Equation 3.39 can be directly deduced from Equation 3.27, by setting $y = 0$. That is

$$G(k_x, y) = \frac{(P + Q)}{N} \tag{3.37}$$

$$G(k_x, -y) = \frac{(P - Q)}{N} \tag{3.38}$$

and

$$G(k_x, 0) = \frac{1}{N} \sum_{k_y=-\frac{N}{2}}^{\frac{N}{2}-1} S(k_x, \hat{k}_y) \tag{3.39}$$

where $y = 1, ..., \frac{N}{2}$ and $k_x = -\frac{N}{2}, ..., \frac{N}{2} - 1$.

When $G(k_x, y)$ is computed for $y = -\frac{N}{2}, ..., \frac{N}{2} - 1$ and $k_x = -\frac{N}{2}, ..., \frac{N}{2} - 1$, direct inverse Fourier transform gives the analytical solution for $m(x, y)$, which represents the motion corrected image, as given in the following equation:

$$m(x, y) = \frac{1}{N} \sum_{k_x=-\frac{N}{2}}^{\frac{N}{2}-1} G(k_x, y) e^{i\frac{2\pi}{N} x k_x} \tag{3.40}$$

3.4.2 Estimation of Angular Velocity

The image reconstruction algorithm described in the previous section assumes that the motion parameter ω_c is known *a priori*. However, in practice, such a measure is difficult to achieve even with the use of sophisticated sensors. Therefore, it is important to be able to estimate ω_c from the acquired data.

Prior to the estimation of ω_c, through iterative or computational technique, it is essential to define a criterion which indicates the degree of error associated with the reconstructed image. For an image with a field of view (FOV) larger than the imaged object, a region of interest (ROI) can be defined using knowledge of the shape of the scanned object. It is also possible to estimate ROI from

the image containing artifacts, as described in Chapter 2. A popular measure of error, associated with the reconstructed image, is the error outside the ROI, denoted by E. Iterative minimization of E can be used to estimate the value of ω_c. The error resulting from a reconstruction using motion parameter value ω_c is given by

$$E = \frac{1}{N^2} \sum_{x=-\frac{N}{2}}^{\frac{N}{2}-1} \sum_{y=-\frac{N}{2}}^{\frac{N}{2}-1} |e_1(x,y)|^2 \tag{3.41}$$

where

$$e_1(x,y) = \begin{cases} m_\omega(x,y) & \text{if } (x,y) \notin \text{ROI} \\ 0 & \text{otherwise} \end{cases}$$

$m_\omega(x,y)$ is the reconstructed image using the motion parameter value ω_c. Although E is a complicated function of ω_c, it is possible to iteratively compute the optimum value of ω_c that minimizes the associated error.

As discussed previously, the total span of rotation can be limited to 180 degrees which corresponds to a maximum angular velocity of 0.01 $\frac{rad}{s}$. Therefore, $\|\omega_c\|$ is bounded within the range 0 and 0.01. Since the constant angular velocity rotation model is symmetric with respect to the object orientation at the acquisition of the $\left(\frac{N}{2}\right)^{th}$ view, only the absolute value of ω_c can be considered.

In order to estimate ω_c, at least two ω_c sweeps are required, each containing a predetermined number of iterations. During the first sweep, ω_c is traversed through the domain in uniform steps to bracket the region containing the global minimum, whereas the second sweep is performed within the bracketed region, in order to isolate the global minimum with the desired accuracy.

3.5 Simulation Results

Simulation experiments were conducted to verify the performance of the proposed algorithms. Shepp & Logan phantom [121], was used as the test object for the simulations (Figure 3.4).

Figure 3.4: Shepp and Logan phantom

3.5.1 Single Step Rotation

In the simulation studies, 3 different cases were examined using simulated MR signals affected by single step rotations. It was assumed that no other movements of the object occur during the course of data acquisition, and no phase errors are induced due to magnetic field inhomogeneity.

The k_{rot} values for each case in the simulation experiments were estimated using the *mismatch function* (DMM), as described in Section 3.3.1. The DMM related to each case is plotted against the phase encoded view pairs (k_y) (see Figure 3.5). Large negative gradients indicate the k_{th} values. The absence of such a gradient indicates the possibility of k_{rot} being either $\left(\frac{N}{2}\right)$ or $\left(\frac{N}{2}\right)+1$. It can also indicate that the data set is not consistent with the single step rotation model.

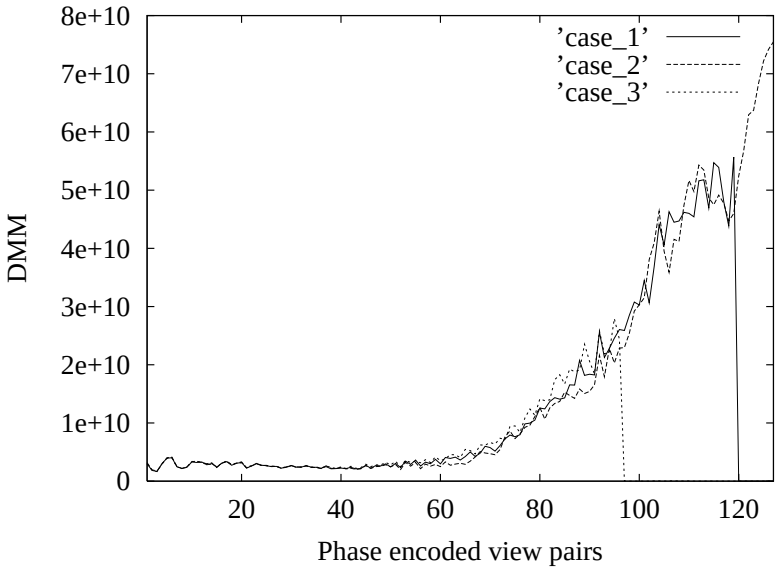

Figure 3.5: Data mismatch function for the 3 simulated data sets.

Experiment number	Set k_{rot}	Option 1		Option 2		selected k_{rot} value
		k_{rot} value	Energy outside ROI	k_{rot} value	Energy outside ROI	
1	120	120	188.706	137	6017.278	120
2	128	128	183.183	129	6852.098	128
3	160	97	3080.698	160	78.600	160

Table 3.1: Resolving k_{rot} value ambiguity using the pixel energy outside the ROI of the reconstructed image.

The ambiguity of the k_{rot} value is then resolved using the pixel energy outside the ROI of the reconstructed image. The ROI boundary for each case was extracted using the algorithm described in Chapter 2. Table 3.1 indicates the energy outside ROI for each possible k_{rot} value and the automatic choice for k_{rot} made by the algorithm. Figures 3.6 to 3.8 illustrate the corrected MR images together with the corresponding motion affected images for comparison.

A relative measure on the quality of the reconstructed image is obtained using

peak signal to noise ratio (PSNR) in the image domain, which is defined by

$$\text{PSNR} = 10 \log_{10} \left[\frac{255^2}{\text{Variance } [n'(x,y)]} \right] dB \tag{3.42}$$

where $n'(x,y) = m^{(I)}(x,y) - m^{(SL)}(x,y)$. $m^{(I)}(x,y)$ is the reconstructed image, whereas $m^{(SL)}(x,y)$ represents the rotated version of the Shepp & Logan phantom [121].

(a) *(b)*

Figure 3.6: Reconstructed images from data set in Case 1, using: *(a)* IFFT (PSNR = 21.233 dB); *(b)* proposed data correction (PSNR = 45.389 dB)

(a) *(b)*

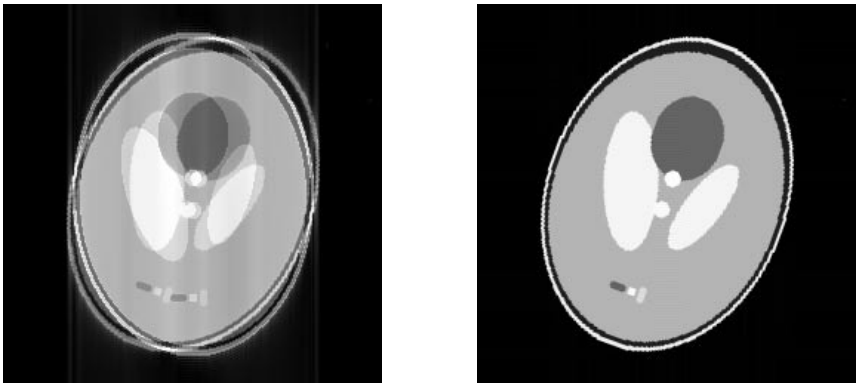

Figure 3.7: Reconstructed images from data set in Case 2, using: *(a)* IFFT (PSNR = 19.080 dB); *(b)* proposed data correction (PSNR = 44.982 dB)

In order to test the noise performance of the proposed algorithm, white Gaussian noise was added to the real and imaginary parts of the simulated MR signal. Although the noise in MRI pixel intensity values follow a Rician distribution [122] [123], the noise in the MRI signal with its separate real and imaginary

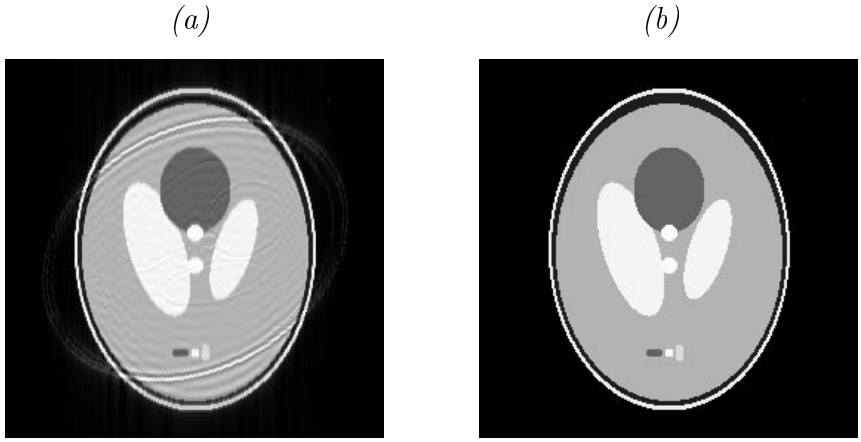

Figure 3.8: Reconstructed images from data set in Case 3, using: *(a)* IFFT (PSNR = 25.878 dB); *(b)* proposed data correction (PSNR = 52.529 dB)

parts is Gaussian in nature [124]. Therefore, the added noise is not Rician, but rather Gaussian. The signal to noise ratio (SNR) of the added noise is set at 16dB for the simulations. The SNR in the k-space is defined as

$$\text{SNR}_{ksp} = 10 \log_{10} \left[\frac{\text{Variance } [S'(k_x, k_y)]}{\text{Variance } [n(k_x, k_y)]} \right] dB \tag{3.43}$$

where $n(k_x, k_y)$ represents the Gaussian noise component.

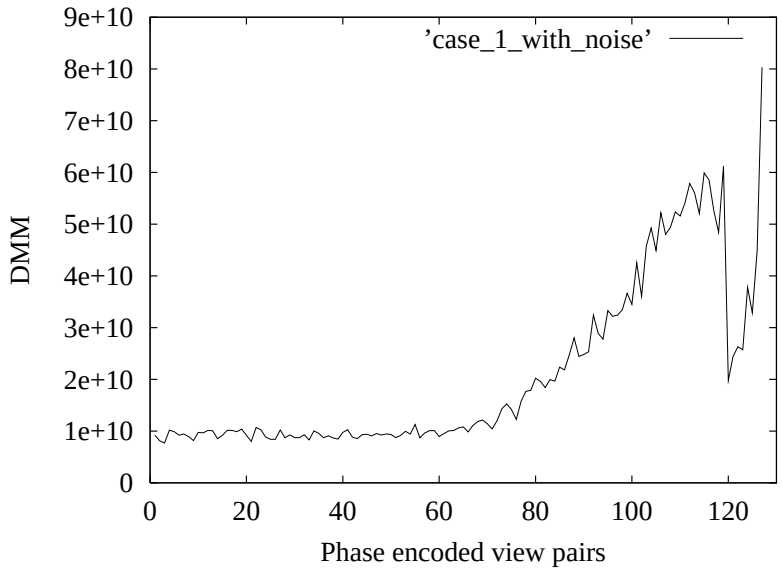

Figure 3.9: Data mismatch function for the Case 1 of the simulated data sets, with added noise.

Figure 3.9 shows the variation of the *mismatch function* (DMM) for the data of

Case 1 with added noise. There is a sufficient negative gradient to indicate the k_{th} value. The k_{rot} value is estimated by minimizing the pixel energy outside ROI. Figure 3.10 illustrate the corrected MR image together with the corresponding motion affected image for comparison.

(a) *(b)*

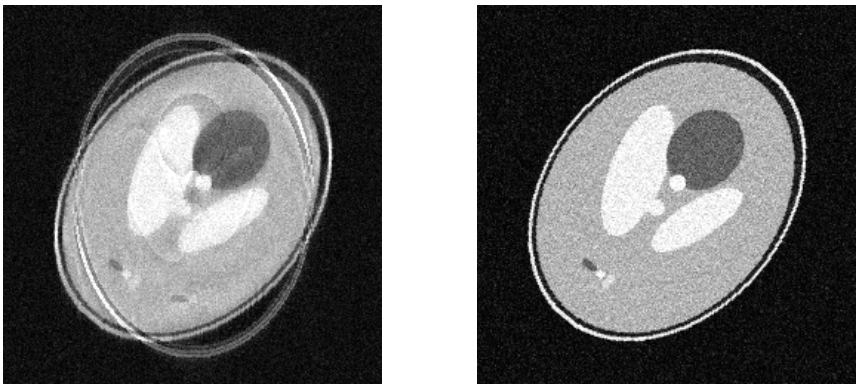

Figure 3.10: Reconstructed images from data set in Case 1 with added noise, using: *(a)* IFFT (PSNR = 20.164 dB); *(b)* proposed data correction (PSNR = 23.894 dB)

The PSNR values of motion affected and motion corrected images for the simulation experiments performed for cases 1 to 3 are tabulated in table 3.2.

Experiment number	PSNR (dB)			
	without noise		with noise (SNR = 16 dB)	
	motion affected	motion corrected	motion affected	motion corrected
1	21.233	45.389	20.164	23.894
2	19.080	44.982	18.374	23.766
3	25.878	52.529	22.984	24.276

Table 3.2: PSNR values of motion affected and motion corrected images for the simulation experiments performed for cases 1 to 3.

It should be noted that although the corrected images display an encouraging improvement on PSNR, for motion satisfying the single step rotation model, the performance of the algorithm is limited by the underlying assumptions. In practice, these assumptions are rarely satisfied. Therefore, data correction using

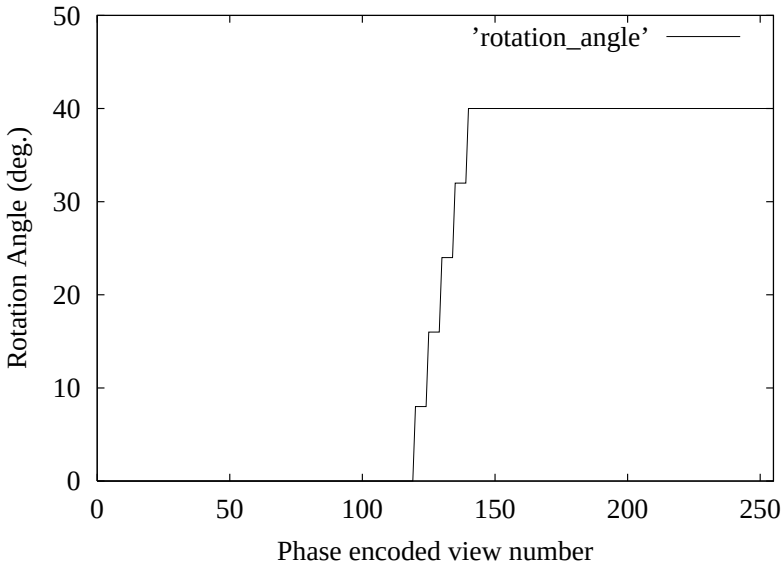

Figure 3.11: Variation of the rotation angle with the view number for rotations where the single step rotation model is marginally violated.

the conjugate symmetry of the k-space data will not be used in the remainder of this thesis. The performance of the algorithm is examined when the single step rotation model is marginally violated. Rotation angles of this simulated motion for each phase encoded view k_y is given in Figure 3.11.

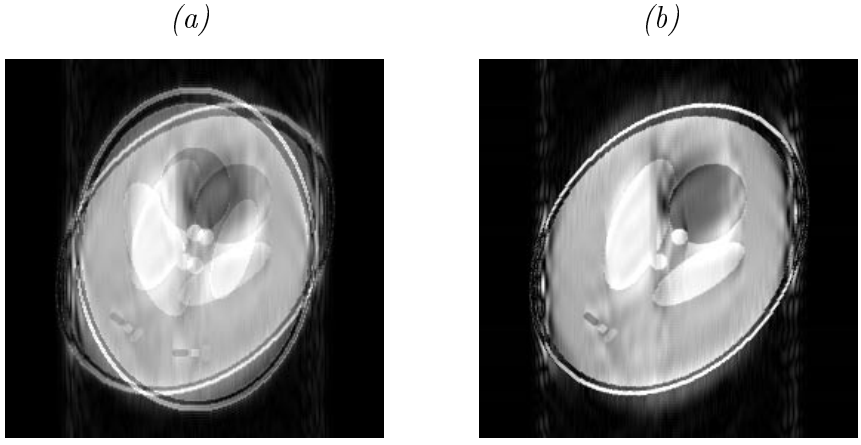

Figure 3.12: Reconstructed images from the data set marginally violating the single step rotation model, using: *(a)* IFFT (PSNR = 16.934 dB); *(b)* proposed data correction (PSNR = 16.135 dB)

The motion corrected image for this case is shown in Figure 3.12, as well as the motion affected image. Notice that the PSNR of the corrected image is

lower than the uncorrected image. The deviation of the data set from the single step rotation model has introduced more artifacts at the data correction stage. Therefore, it is clear that the correction method used is highly sensitive to the motion model.

3.5.2 Rotation at Constant Angular Velocity

In the simulation studies for rotation at constant angular velocity, the object is assumed to undergo rotational motion at a constant or near constant angular velocity. The rotations are constrained around the slice selection axis, within the imaging plane. In each simulation experiment, a fixed repetition time (T_R) of 1000ms is used. The echo time (T_e) is 30ms. A total of 256 phase encoding steps are performed for each experiment. 1024 samples are acquired at each phase encoding step with $20\mu s$ sampling period (i.e. $m = 4$). Hence the total data acquisition period per phase encoding MR signal amounts to 20.5ms. Gaussian white noise is added to the real and imaginary parts of the simulated MR signal, to test the noise performance of the proposed algorithm. The signal to noise ratio (SNR) of the added noise is set to 16dB.

(a) *(b)* *(c)*

Figure 3.13: Reconstructed images (10^o span) using *(a)* IFFT (PSNR=22.23), *(b)* BSA (PSNR=24.67) and *(c)* Proposed algorithm (PSNR=25.69)

The conventional inverse Fourier transform image reconstruction technique [5]

was applied to the MR signal taken from the rotating object. The resulting image is observed to contain ghosting and blurring artifacts. The ROI of the image is estimated using the method described in Chapter 2.

The constant angular velocity (ω_c) is estimated directly using the MR signal data with the aid of two consecutive ω_c sweeps. The iterative procedure converges successfully to the desired solution with less than 5% error, at 16dB SNR noise level. The image reconstruction is performed using the analytical method described in Section 3.4.1.

(a) *(b)* *(c)*

Figure 3.14: Reconstructed images (20^o span) using *(a)* IFFT (PSNR=20.75), *(b)* BSA (PSNR=24.39) and *(c)* Proposed algorithm (PSNR=25.63)

(a) *(b)* *(c)*

Figure 3.15: Reconstructed images (40^o span) using *(a)* IFFT (PSNR=17.82), *(b)* BSA (PSNR=24.21) and *(c)* Proposed algorithm (PSNR=25.47)

Figures 3.13 to 3.16 illustrate four different simulation results with total rotations

(a) *(b)* *(c)*

Figure 3.16: Reconstructed images (140^o span) using *(a)* IFFT (PSNR=16.34), *(b)* BSA (PSNR=22.70) and *(c)* Proposed algorithm (PSNR=23.88)

of 10^o, 20^o, 40^o and 140^o which span through the allowable range of 0^o to 180^o. In each case, an image quality improvement of over 80% is achieved. The results also indicate that the proposed analytical method performs better than the bilinear superposition algorithm (BSA) [78], which will be discussed in Chapter 5.

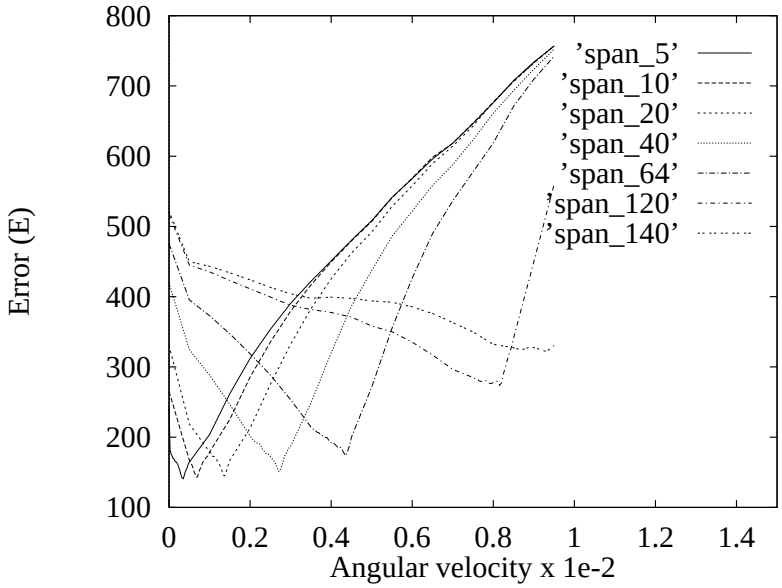

Figure 3.17: Variation of error (E) with the angular velocity ω_c.

Figure 3.17 illustrates the Error (E) variation with angular velocity, for the cases described in Table 3.3. It should be noted that angular spans of less than 5^o produce little effect due to the presence of noise at 16dB SNR, which effectively

overshadows the motion artifacts. The ω_c value at each global minimum is chosen to be the estimated motion parameter associated with the corresponding experiment.

Experiment number	Rotational span	set ω_c (r/s)	Estimated ω_c (r/s)	% estimation error
1	5^o	0.3409e-3	0.3500e-3	2.67
2	10^o	0.6818e-3	0.6750e-3	1.00
3	20^o	1.3635e-3	1.3750e-3	0.84
4	40^o	2.7271e-3	2.7000e-3	0.99
5	64^o	4.3633e-3	4.3500e-3	0.30
6	120^o	8.1812e-3	8.1500e-3	0.38
7	140^o	9.5448e-3	9.3000e-3	2.56

Table 3.3: Parameter estimation results for rotation at constant angular velocity.

Figure 3.18 shows a comparison of the final image quality, when reconstructed using conventional IFFT, bilinear superposition algorithm (BSA) [78] and the algorithm proposed in this chapter.

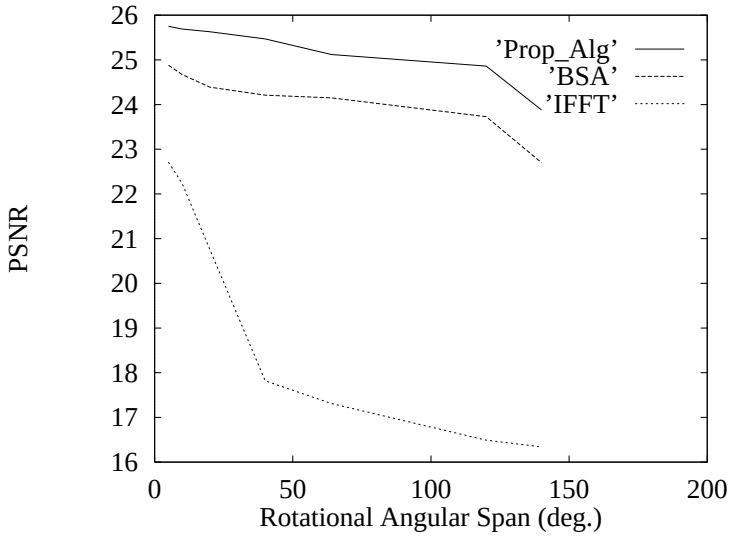

Figure 3.18: Reconstructed image quality comparison

It should be noted that, the proposed algorithm is based on the constant angular velocity rotation model, and hence, significant deviations from this model result

in residual artifacts in the reconstructed image. In order to quantify the effects of deviation from the set constant-angular velocity rotational model, rotations at time-varying angular velocities were considered. The rotations involved accelerations and decelerations in angular velocity for angular spans of 10^o, 20^o, 40^o and 80^o, as shown in Figure 3.19.

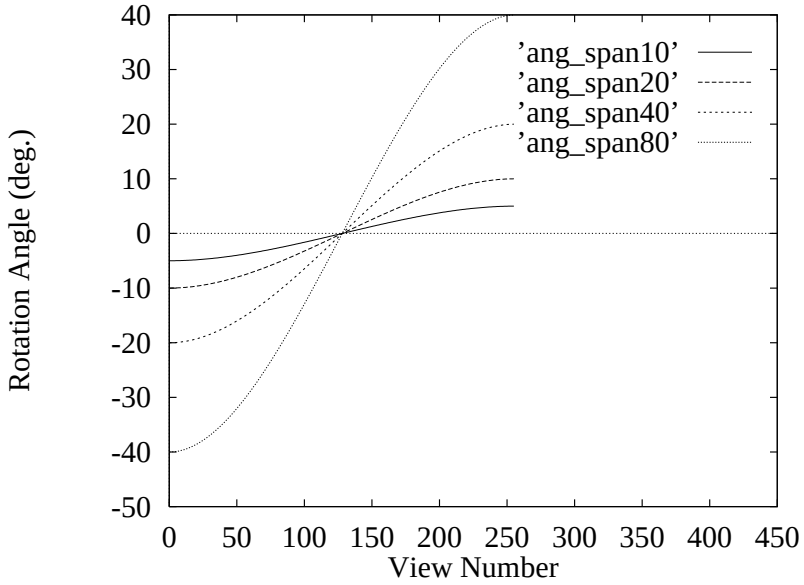

Figure 3.19: Variation of rotation angle with the view number for rotations involving time varying angular velocities (i.e. acceleration / deceleration).

A comparison of the final image quality, when reconstructed using direct IFFT, BSA and the proposed algorithm is given in Table 3.4, with corresponding PSNR and the number of computations involved.

Method	Computations	PSNR for angle spans of			
		10^o	20^o	40^o	80^o
IFFT	2,048	18.36	18.08	17.40	16.49
BSA	570,425,344	24.53	24.31	24.15	23.77
Prop. Alg.	788,480	25.10	24.64	24.15	19.65

Table 3.4: Reconstructed image quality comparison for model mismatch

It was observed that, for small angular spans, the constant angular velocity model is a close approximation for the actual rotations, producing insignificant artifacts

due to model mismatch. However, at larger angular spans, the model mismatch becomes pronounced, producing visible artifacts in the reconstructed image, as shown in Figure 3.20.

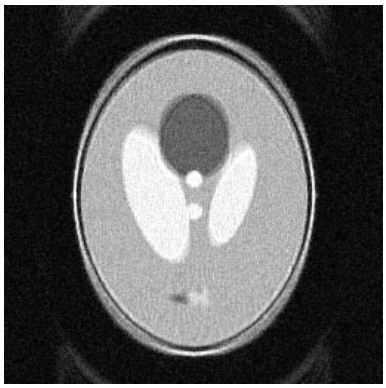

Figure 3.20: Visible artifacts in the reconstructed image, due to motion model mismatch. (Rotational angular span = 80^o)

The total computations involved in the reconstruction process can be categorized into N^2 bilinear interpolations, N^2 computations of $G(k_x, y)$ values and a 1D IFFT. Bilinear interpolations along the view data in the k-space involve computation of N^2 complex values, provided that the number of phase encodes is N. According to Equations 3.22 and 3.23, each computation involves 2 multiplications for real and imaginary parts of $D(\hat{i}, k_y)$ and 3 multiplications to evaluate $\hat{i}$. Therefore, the total multiplications involved in the interpolation stage amounts to $5N^2$.

Computation of $G(k_x, y)$ involves $7N^2$ multiplications according to Equations 3.26 to 3.34 which include the calculation of $\hat{k}_y$. The final stage is a single 1D IFFT which involves $Nlog_2N$ multiplications. Therefore, the total operations amount to $O(12N^2 + Nlog_2N)$.

The bilinear superposition algorithm [78] involves $2N$ forward and inverse 2D Fourier transforms, together with N 2D bilinear interpolations, each involving N^2 complex values. The total computations involved in Fourier transforms amount

to $2N \times N^2 log_2 N^2 (= 4N^3 log_2 N)$, and the bilinear interpolations add a further $N \times 2N^2 (= 2N^3)$ computations. Therefore, the total operations involved amount to $O(2N^3 + 4N^3 log_2 N)$. When $N = 256$, the proposed algorithm involves 788480 operations to reconstruct the image, whereas the bilinear superposition algorithm [78] needs 570425344 operations.

Therefore, the final image can be computed in $O(12N^2 + N log_2 N)$ operations, if there are N phase encoding steps. Compared to the bilinear superposition algorithm [78], which involves $O(2N^3 + 4N^3 log_2 N)$ operations, the proposed algorithm is more efficient. Both the above methods are more efficient than the method proposed by Atalar et al.[84] which involves 257 singular value decompositions (SVD) [75].

The image reconstruction times using the proposed correction model for single step rotation varies from 8 minutes to 12.5 minutes on a Sun SPARC 2 workstation, with most time (i.e. approximately 90%) consumed at the k_{rot} estimation stage. On the same workstation, the reconstruction times using the proposed correction model for constant angular velocity varies from 10.5 minutes to 16 minutes, with approximately 85% of the processing time consumed at the estimation of ω_c.

3.6 Summary

A general model for in-plane rotational motion has been developed in this Chapter. In order to consider the simplest case, a single step rotation model was considered initially. However, this model is limited by unrealistic assumptions that are rarely satisfied in practice. Rotations at constant angular velocity is considered next, which relax the stringent constraints imposed in the single step rotation model. An analytical artifact suppression method, that does not rely on

the conjugate symmetry of the k-space data, has been presented for this type of motion. The rotations are still constrained within the imaging plane. The simulation results indicate that interpolation along inclined lines of acquired view data, as opposed to the interpolation on to the nearest k-space grid points as used in BSA [78], result in a quality improvement in the reconstructed images. The proposed method successfully suppresses artifacts, even if the rotations involve large angles. The algorithm is shown to be more computationally efficient compared to the methods of rotational motion artifact cancellation proposed in past literature [7][80][78], provided that the data corruption satisfies the constant angular velocity rotation model. It is also shown to be possible to estimate the motion parameter from the corrupted data, using error minimization outside the ROI. The successful performance of the estimation method and the image reconstruction algorithm has been proven, in the presence of noise, using simulation results.